Incorporation of Anisotropic Scattering in nTRACER

Min Ryu, Yeon Sang Jung, Chang Hyun Lim and Han Gyu Joo *
Seoul National University, 1 Gwanak-ro, Gwanak-gu, Seoul, 151-744, Korea
**Corresponding author: joohan@snu.ac.kr*

1. Introduction

Proper treatment of anisotropic scattering is one of the major issues in developing Method of Characteristic (MOC) codes. As the typical method, the isotropic scattering scheme with the transport-corrected scattering cross section is commonly used. The transport-corrected scattering cross section generated with out-scattering conservation yield good enough solutions in most circumstances. However, this isotropic treatment with out-scattering based transport correction [1] is not desirable particularly when there appear high neutron currents due to a strong absorber or the large leakage near the core periphery. Instead of the out-scattering based transport correction, the in-scattering transport correction [1] can be used or an explicit treatment of anisotropic scattering with angular flux moments can be remedies in such cases.

In the direct whole core transport code developed at Seoul National University, nTRACER [2], only out-scattering based isotropic scattering treatment was available and degradation of accuracy was noticed while solving the recent highly detailed and realistic pressurized water reactor (PWR) benchmark problems, namely, the BEAVRS[3] and the VERA[4] benchmarks which were proposed by the Computational Reactor Physics Group (CRPG) of MIT and the CASL (Consortium for Advanced Simulation of Light water reactors) group at the Oak Ridge National Laboratory (ORNL). This work is to implement the anisotropic scatter treatment capability in nTRACER and also to generate properly the in-scattering based transport cross section, and then to examine the performance of the improved anisotropic scattering treatments.

2. In-scattering Transport Correction

The out-scattering based transport correction is to define the transport cross section as follows:

$$\Sigma_{tr,g} = \Sigma_{t,g} - \sum_{g'} \Sigma^{(1)}_{s,g\to g'} \quad . \tag{1}$$

This definition comes from the inconsistent P1 approximation that equates the in-scattering source and out-scattering source for a group. For more faithful generation of transport cross section without employing that approximation, let us first consider the equation for the first moment in a one-dimensional geometry as:

$$\frac{1}{3}\frac{\partial}{\partial z}\phi_g(z) + \Sigma_{t,g} J_g(z) = \sum_{g'} \Sigma^{(1)}_{s,g'\to g} J_{g'}(z) \quad . \tag{2}$$

By introducing the Fick's law that involves the group diffusion coefficient which is assumed to be unknown in the following derivation, Eq. (2) can be rewritten as follows:

$$\frac{1}{3}\frac{\partial}{\partial z}\phi_g(z) - \Sigma_{t,g} D_g \frac{\partial}{\partial z}\phi_g(z) = -\sum_{g'} \Sigma^{(1)}_{s,g'\to g} D_{g'} \frac{\partial}{\partial z}\phi_{g'}(z) \quad . \tag{3}$$

Eq. (3) can be integrated in an arbitrary interval to yield:

$$\frac{1}{3}\phi_g - \Sigma_{t,g} D_g \phi_g = -\sum_{g'} \Sigma^{(1)}_{s,g'\to g} D_{g'} \phi_{g'} \quad . \tag{4}$$

Eq. (4) represents a system of linear equation that can be solved for D_g for a given spectrum. A typical spectrum in a PWR can be used in Eq. (4) and the resulting solution for D_g can be used to determine the transport cross section as:

$$\Sigma_{tr,g} = \frac{1}{3D_g} \quad . \tag{5}$$

3. MOC with high order scattering

In the typical MOC calculation, scattering sources are treated isotropic and thus only the scalar flux needs to be stored at each flat source region. However, with the high order scattering source expansion method, higher order scattering moments are required. These higher moments are explicitly derived from the expansion of angular flux in terms of the spherical harmonics given as:

$$Y_{lm}(\mu,\alpha) = \sqrt{\frac{(l-m)!}{(l+m)!}} P_l^m(\mu)\exp(im\alpha), \mu = \cos\theta \quad . \tag{6}$$

The high order flux moment is defined as follows:

$$\phi_l^m(\mathbf{r},E') = \int_{-1}^{1} d\mu' \int_0^{2\pi} d\alpha' \varphi(\mathbf{r},E',\hat{\Omega}') Y^*_{lm}(\mu',\alpha') \quad . \tag{7}$$

The 0-th order scattering source can then be expressed as follows:

$$\begin{aligned} S_{00}(\mathbf{r},E,\hat{\Omega}) &= \frac{1}{4\pi}\int_{E'} dE' \Sigma_s^{(0)}(\vec{r},E'\to E)\phi_0^0(\mathbf{r},E') Y_{00}(\mu,\alpha) \\ &= \frac{1}{4\pi}\int_{E'} dE' \Sigma_s^0(\mathbf{r},E'\to E)\int_{-1}^{1} d\mu' \int_0^{2\pi} d\alpha' \varphi(\mathbf{r},E',\hat{\Omega}') \\ &= \frac{1}{4\pi}\int_{E'} dE' \Sigma_s^0(\mathbf{r},E'\to E)\phi(\mathbf{r},E') \end{aligned} \quad . \tag{8}$$

The higher order scattering source can also be derived as the following up to the third order in terms of the

higher order moments that should be calculated during the ray tracing calculation employing the MOC:

1-st order

$$\begin{aligned}&S_1(\mathbf{r},E,\hat{\Omega}) = S_{10}(\mathbf{r},E,\hat{\Omega}) + S_{1,-1}(\mathbf{r},E,\hat{\Omega}) + S_{11}(\mathbf{r},E,\hat{\Omega})\\&= \frac{3}{4\pi}\int_{E'} dE'\Sigma_s^{(1)}(\mathbf{r},E'\to E)\int_{-1}^{1}\int_0^{2\pi}\big(\ \cos\theta'\cos\theta\\&+\sin\theta'\sin\theta\cos\alpha'\cos\alpha+\sin\theta'\sin\theta\sin\alpha'\sin\alpha\ \big)\\&\varphi(\mathbf{r},E',\hat{\Omega}')d\alpha' d\mu'\end{aligned} \quad . \qquad (9)$$

2-nd order

$$\begin{aligned}&S_2(\mathbf{r},E,\hat{\Omega}) = S_{20}(\mathbf{r},E,\hat{\Omega}) + S_{2,-1}(\mathbf{r},E,\hat{\Omega})\\&+S_{21}(\mathbf{r},E,\hat{\Omega}) + S_{2,-2}(\mathbf{r},E,\hat{\Omega}) + S_{22}(\mathbf{r},E,\hat{\Omega})\\&= \frac{5}{4\pi}\int_{E'} dE'\Sigma_s^{(2)}(\mathbf{r},E'\to E)\int_{-1}^{1}\int_0^{2\pi}\\&\left[\begin{array}{l}\left[\frac{1}{2}(3\cos^2\theta'-1)\right]\cdot\left[\frac{1}{2}(3\cos^2\theta-1)\right]\\+3\cos\theta'\cos\theta\sin\theta'\sin\theta\cos\alpha'\cos\alpha\\+3\cos\theta'\cos\theta\sin\theta'\sin\theta\sin\alpha'\sin\alpha\\+\frac{3}{4}\sin^2\theta'\sin^2\theta\cos(2\alpha')\cos(2\alpha)\\+\frac{3}{4}\sin^2\theta'\sin^2\theta\sin(2\alpha')\sin(2\alpha)\end{array}\right]\\&\varphi(\mathbf{r},E',\hat{\Omega}')d\alpha' d\mu'\end{aligned} \quad . \qquad (10)$$

3-rd order

$$\begin{aligned}&S_3(\mathbf{r},E,\hat{\Omega}) = S_{30}(\mathbf{r},E,\hat{\Omega}) + S_{3,-1}(\mathbf{r},E,\hat{\Omega}) + S_{31}(\mathbf{r},E,\hat{\Omega})\\&+S_{3,-2}(\mathbf{r},E,\hat{\Omega}) + S_{32}(\mathbf{r},E,\hat{\Omega}) + S_{3,-3}(\mathbf{r},E,\hat{\Omega}) + S_{33}(\mathbf{r},E,\hat{\Omega})\\&= \frac{7}{4\pi}\int_{E'} dE'\Sigma_s^{(3)}(\vec{\mathrm{r}},E'\to E)\int_{-1}^{1}\int_0^{2\pi}\\&\left[\begin{array}{l}\left[\frac{1}{2}(5\cos^3\theta'-\cos\theta')\right]\cdot\left[\frac{1}{2}(5\cos^3\theta-\cos\theta)\right]\\+\frac{3}{8}(5\cos^2\theta'-1)\sin\theta'(5\cos^2\theta-1)\sin\theta\cos\alpha'\cos\alpha\\+\frac{3}{8}(5\cos^2\theta'-1)\sin\theta'(5\cos^2\theta-1)\sin\theta\sin\alpha'\sin\alpha\\+\frac{15}{4}\cos\theta'\sin^2\theta'\cos\theta\sin^2\theta\cos(2\alpha')\cos(2\alpha)\\+\frac{15}{4}\cos\theta'\sin^2\theta'\cos\theta\sin^2\theta\sin(2\alpha')\sin(2\alpha)\\+\frac{5}{8}\sin^3\theta'\sin^3\theta\cos(3\alpha')\cos(3\alpha)\\+\frac{5}{8}\sin^3\theta'\sin^3\theta\sin(3\alpha')\sin(3\alpha)\end{array}\right]\\&\varphi(\mathbf{r},E',\hat{\Omega}')d\alpha' d\mu'\end{aligned} \quad . \qquad (11)$$

Note that the terms containing the trigonometric function need to be multiplied to the angular flux for a certain angle and then accumulated to define the proper moment during the ray tracing calculation and this calculation induces a significant increase in the computing time.

4. Examination of Effectiveness

In order to examine the effectiveness of the anisotropic scattering treatments, the upgraded nTRACER was applied to the VERA and the BEAVRS benchmark problems. nTRACER's own 47-group cross section library generated from the ENDF-B/VII data were used and contains the in-scattering based transport cross section generated for primary light nuclides such as H-1, B-10 and O-16 were used. The ray spacing used in nTRACER is 0.05 cm except for the Integral Fuel Burnable Absorber (IFBA) cases for which it is set to 0.01 cm. The numbers of azimuthal angles and optimum polar angles per octant of the solid angle sphere are 12 and 4 for all the cases except for the IFBA cases having 16 azimuthal angles.

3.1. VERA benchmark Analysis

For the VERA benchmark problem, the reference solutions obtained by the KENO-VI Monte Carlo (MC) code are given. There are several kinds of two-dimensional (2D) problems and they are used in the following examination of various scattering treatment cases.

3.1.1 2D Lattice problems

There are a total of 17 different kinds of 2D lattice problems in the VERA benchmark. These assemblies are standard Westinghouse 17x17 assemblies. As shown in Table I, higher order scattering results such as P1, P2 and P3 show better performance in the case of no poison lattice. P2 gives more accurate results than P1 and the k-effective values and the pin power distributions of P2 are almost the same as those of P3.

Table I. VERA 2D lattices with no poison

No	Descrip-Tion	Code	k-effective	$\Delta\rho$	Pin Max Error
2A	None 565K/565K 0.743 g/cc	KENO-VI	1.18218(3)	-	-
		Out-scat.	1.18089	-92	0.21%
		In-scat.	1.18091	-91	0.33%
		P1	1.18125	-66	0.17%
		P2	1.18149	-49	0.16%
		P3	1.18146	-51	0.16%
2B	None 600K/600K 0.661 g/cc	KENO-VI	1.18336(3)	-	-
		Out-scat.	1.18252	-60	0.21%
		In-scat.	1.18251	-61	0.33%
		P1	1.18265	-51	0.18%
		P2	1.18290	-33	0.18%
		P3	1.18287	-35	0.18%
2C	None 900K/600K 0.661 g/cc	KENO-VI	1.17375(3)	-	-
		Out-scat.	1.17260	-84	0.17%
		In-scat.	1.17261	-83	0.29%
		P1	1.17268	-78	0.15%
		P2	1.17295	-58	0.14%
		P3	1.17286	-65	0.14%
2D	None 1200K/600K 0.661 g/cc	KENO-VI	1.16559(3)	-	-
		Out-scat.	1.16416	-105	0.20%
		In-scat.	1.16417	-105	0.33%
		P1	1.16419	-103	0.17%
		P2	1.16447	-83	0.17%
		P3	1.16432	-94	0.17%
2I	IT	KENO-VI	1.17992(2)	-	-

	600K/600K 0.661 g/cc	Out-scat.	1.17868	-89	0.22%
		In-scatt.	1.17868	-89	0.34%
		P1	1.17904	-63	0.17%
		P2	1.17926	-47	0.17%
		P3	1.17923	-49	0.17%

Table II shows the results of the four cases of Pyrex shimmed problems. On the contrary to the prior case, the out-scattering treatment seems to give the best solution, but this is due to some error cancelation effects. The Pn cases show consistently better results as the order increases revealing the general trend of the zigzag variation in the error as the order increases.

Table II. VERA 2D lattices with Pyrex

No	Descrip-Tion	Code	k-effective	$\Delta\rho$	Pin Max Error
2E	12 Pyrex	KENO-VI	1.06963(2)	-	-
		Out-scat.	1.06922	-36	0.21%
		In-scat.	1.06847	-101	0.22%
		P1	1.06828	-118	0.26%
		P2	1.06881	-71	0.22%
		P3	1.06876	-76	0.22%
2F	24 Pyrex	KENO-VI	0.97602(3)	-	-
		Out-scat.	0.97610	9	0.24%
		In-scat.	0.97486	-122	0.48%
		P1	0.97452	-157	0.30%
		P2	0.97522	-84	0.30%
		P3	0.97515	-91	0.29%
2J	IT + 24 Pyrex	KENO-VI	0.97519(3)	-	-
		Out-scat.	0.97535	17	0.17%
		In-scat.	0.97411	-114	0.36%
		P1	0.97377	-150	0.20%
		P2	0.97448	-75	0.22%
		P3	0.97440	-83	0.21%
2K	Radially Zoned + 24 Pyrex	KENO-VI	1.02006(3)	-	-
		Out-scat.	1.02031	24	0.22%
		In-scat.	1.01912	-91	0.43%
		P1	1.01882	-120	0.27%
		P2	1.01952	-52	0.25%
		P3	1.01944	-60	0.25%

There are two control rod (CR) insertion cases in the second problem set. The neutron flux distribution in the assembly changes drastically because of the high absorbers. Due to the large neutron currents formed near the absorber, the out-scattering based transport correction yields very large errors in the eigenvalue as shown in Table III. The improvement with the high order scattering treatment is remarkable both in Table III and Fig. 1. Although in-scattering based transport correction improves the eigenvalue significantly, it is noted that the power distribution error is degraded slightly.

Table III. VERA benchmark – 2D Lattice with CR

No	Descrip-Tion	Code	k-effective	$\Delta\rho$	Pin Max Error
2G	24 AIC (Ag-In-Cd)	KENO-VI	0.84770(3)	-	-
		Out-scattering	0.85085	437	0.40%
		In-scattering	0.84860	126	0.91%
		P1	0.84557	-296	0.27%
		P2	0.84777	10	0.27%
		P3	0.84765	-6	0.28%
2H	24 B_4C	KENO-VI	0.78822(3)	-	-
		Out-scattering	0.79295	760	0.43%
		In-scattering	0.78793	-47	1.05%
		P1	0.78547	-444	0.39%
		P2	0.78855	53	0.35%
		P3	0.78847	40	0.38%

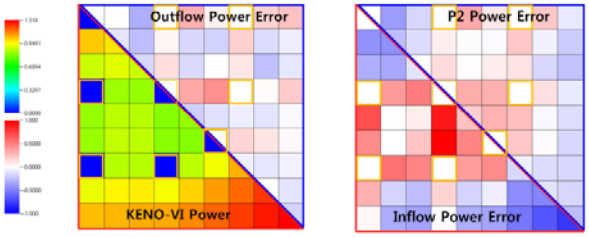

Fig. 1. Pin power distribution of the 2H case and relative errors with various transport correction and the P2 MOC method

As shown in Table IV and V which are for the cases with IFBA, gadolinium and Zircarloy grids, high order scattering treatment give the best accuracy, but not so obviously as the CR cases. Fig. 2 summarized the reactivity errors for the assembly cases.

Table IV. VERA benchmark – 2D Lattice with IFBA

No	Descrip-Tion	Code	k-effective	$\Delta\rho$	Pin Max Error
2L	80 IFBA	KENO-VI	1.01892(2)	-	-
		Out-scat.	1.01654	-229	0.29%
		In-scat.	1.01625	-257	0.29%
		P1	1.01681	-203	0.17%
		P2	1.01703	-182	0.14%
		P3	1.01700	-185	0.14%
2M	128 IFBA	KENO-VI	0.93880(3)	-	-
		Out-scat.	0.93599	-319	0.30%
		In-scat.	0.93565	-358	0.33%
		P1	0.93636	-277	0.15%
		P2	0.93655	-255	0.12%
		P3	0.93652	-259	0.12%
2N	104 IFBA 20 WABA	KENO-VI	0.86962(3)	-	-
		Out-scat.	0.86881	-107	0.38%
		In-scat.	0.86755	-274	0.31%
		P1	0.86796	-219	0.18%
		P2	0.86843	-157	0.14%
		P3	0.86838	-164	0.14%

Table V. VERA benchmark – 2D Lattice with Gd and Zircarloy Grid

No	Descrip-Tion	Code	k-effective	$\Delta\rho$	Pin Max Error
2O	12 Gd	KENO-VI	1.04773(2)	-	-
		Out-scat.	1.04907	122	5.43%
		In-scat.	1.04822	45	5.84%
		P1	1.04741	-29	6.39%
		P2	1.04813	37	5.98%
		P3	1.04806	30	6.02%
2P	24 Gd	KENO-VI	0.92741(2)	-	-
		Out-scat.	0.92895	179	5.33%
		In-scat.	0.92782	48	5.66%
		P1	0.92616	-146	6.27%
		P2	0.92718	-27	5.86%
		P3	0.92707	-40	5.90%
2Q	Zir Grid	KENO-VI	1.17194(2)	-	-

		Out-scat.	1.17157	-27	0.36%
		In-scat.	1.17154	-29	0.42%
		P1	1.17188	-4	0.39%
		P2	1.17215	15	0.38%
		P3	1.17212	13	0.38%

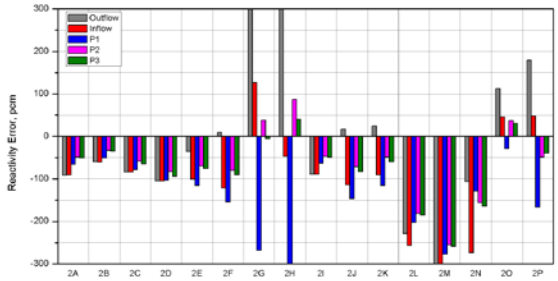

Fig. 2. k-effective errors of each method for the VERA 2D lattice problems

3.1.2 2D 3x3 mini-core

In the VERA 3x3 mini-core problem with the reflective boundary condition, the center assembly can have three control rod insertion conditions: A) with no control rod, B) AIC control rod in, C) B_4C control rod in. Fig. 3 shows the core configuration of the 3x3 mini-core. As shown in Table VI, the improvement with the higher order scattering and the in-scattering treatment is quite significant in both reactivity and power distribution. The in-scattering correction improves the power distribution as well in these 3x3 mini-core cases.

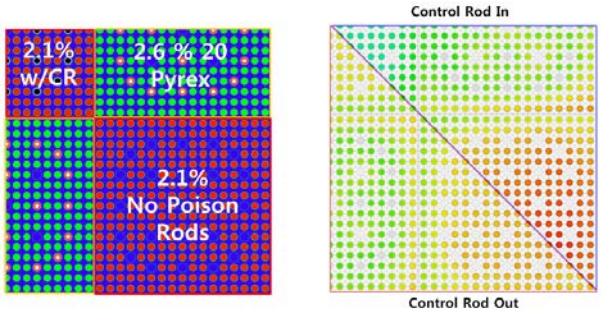

Fig. 3. Configuration of VERA 2D 3x3 mini-core

Table VI. VERA benchmark – 2D 3x3 mini-core

No	Descrip-tion	Code	k-effective	$\Delta\rho$	Pin Max Error	Rod Worth & Error
4A	None	KENO-VI	1.01024(1)	-	-	-
		Out-scat.	1.00905	-117	0.47%	
		In-scat.	1.00847	-174	0.73%	
		P1	1.00862	-159	0.37%	
		P2	1.00903	-119	0.33%	
		P3	1.00898	-123	0.33%	
4B	AIC	KENO-VI	0.98345(1)	-	-	2697(2)
		Out-scat.	0.98241	-107	2.01%	-9
		In-scat.	0.98194	-156	1.41%	-18
		P1	0.98168	-183	0.41%	24
		P2	0.98229	-120	0.45%	1
		P3	0.98224	-125	0.62%	1
4C	B_4C	KENO-VI	0.98029(1)	-	-	3024(2)
		Out-scat.	0.97918	-116	2.38%	-1
		In-scat.	0.97870	-166	1.59%	-8
		P1	0.97847	-190	0.42%	31
		P2	0.97914	-120	0.59%	1
		P3	0.97909	-125	0.62%	2

Fig. 4. Errors of pin power distribution of the 4C case with various transport corrections, P1 and P2 MOC method

3.1.3 2D quarter core

The 2D quarter core cases are similar to the previous 3x3 mini-core cases in that they are HZP problems with three different control rod conditions. In these cases, however, there is large neutron leakage so the anisotropic effect near problem boundary is not negligible. As shown in Table VII, Figs. 5 and 6, the out-scattering transport correction involves a significant radial power tilt that causes a very large power error at the core center. The higher order scattering and the in-scattering correction are very much effective in these core cases.

Table VII. VERA benchmark – 2D quarter core

No	Descrip-tion	Code	k-effective	$\Delta\rho$	Asy Max Error	Rod Worth & Error
5A	None	KENO-VI	1.00409(1)	-	-	-
		Out-scat.	1.00185	-222	5.40%	
		In-scat.	1.00248	-159	1.57%	
		P1	1.00220	-187	1.19%	
		P2	1.00272	-136	0.70%	
		P3	1.00267	-141	0.72%	
5B	AIC	KENO-VI	0.99150(1)	-	-	1265(1)
		Out-scat.	0.98905	-249	9.57%	27
		In-scat.	0.98980	-173	1.52%	13
		P1	0.98954	-187	1.72%	12
		P2	0.99018	-134	1.10%	-2
		P3	0.99013	-139	1.11%	-1
5C	B_4C	KENO-VI	0.98029(1)	-	-	1394(1)
		Out-scat.	0.98767	-261	10.01%	39
		In-scat.	0.98849	-177	1.52%	18
		P1	0.98818	-209	1.95%	22
		P2	0.98885	-141	1.28%	5
		P3	0.98880	-146	1.30%	5

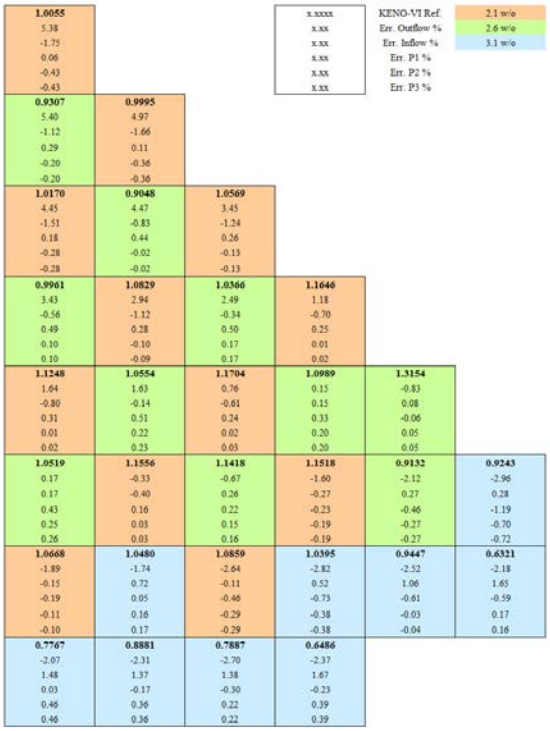

Fig. 5. Reference assembly power and relative error distributions of each method for the VERA 5A case (ARO)

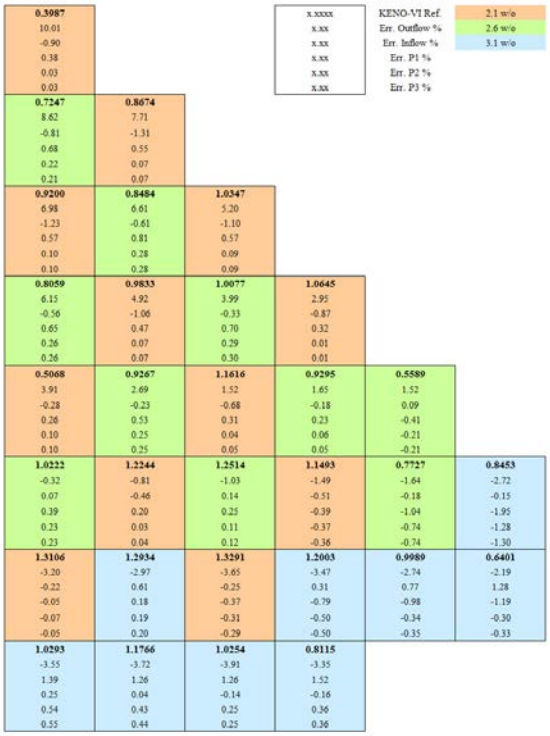

Fig. 6. Reference assembly power and relative error distributions of each method for the VERA 5C case (Bank D with B4C inserted)

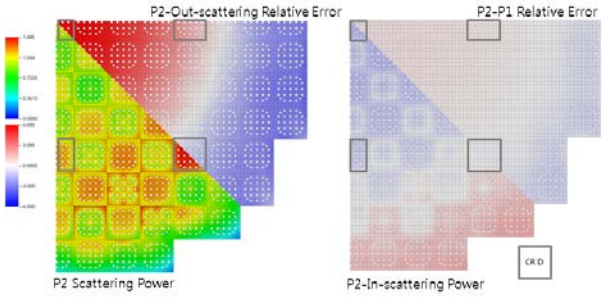

Fig. 7. Pin power distribution with P2 MOC and relative differences between each method and P2 for the VERA 5A case

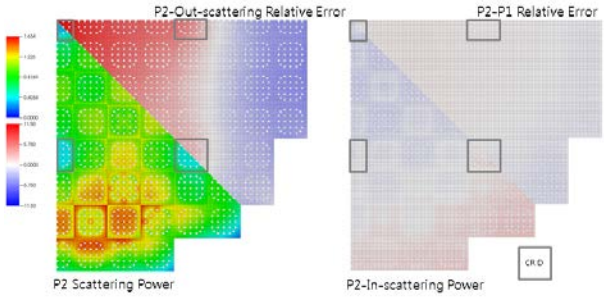

Fig. 8. Pin power distribution with P2 MOC and relative differences between each method and P2 for the VERA 5C case

3.2. BEAVRS benchmark

In the BEAVRS benchmark problem, the power distribution information was obtained by in-core detector measurements. As in the VERA 2D problems, the 3D quarter core problem also has large neutron leakage so that the anisotropic effect near the core baffle is not negligible. As shown in Table VIII and Fig. 9, the out-scattering transport correction also involves a significant radial power tilt similarly to the VERA 2D quarter cores. The high order scattering and the in-flow scattering correction improve the radial assembly power distribution quite noticeably as well in this BEAVRS core by removing the power tilt resulting in an over-estimation at the interior when the out-scattering based transport cross sections are used. Due to the less leakage obtained with the better anisotropic scattering treatment, the core k-effective increases by about 110 pcm. Conversely, this indicates that out-scattering based cross sections induces too much leakage. This is confirmed by the lower transport cross sections of hydrogen at the high energy range in Fig. 10. The smaller cross sections for high energy neutrons would lead to large mean free paths that will cause more leakage. The higher leakage would induce the radial power tilt in such a way that the power is over-predicted in the interior region.

As far as the computing time is concerned, however, the P2 calculation requires a significantly more computing time than the in-scattering based calculation time that is essentially the same as the out-scattering based one. With 168 computing nodes, the time for this

BEAVRS calculation with P2 was about 6 hours whereas it was about 2 hours and 45 minutes with the isotropic scattering. Since the in-scattering based results are not so bad compared with the P2 calculation, it might be beneficial to perform the in-scattering based transport calculation in most calculations.

Table. VIII BEAVRS Benchmark 3D HZP k-effective

Methods	Out-scattering	In-scattering	P2
k-effective	0.99967	1.00082	1.00078
Asy. RMS error	3.40%	2.84%	2.75%

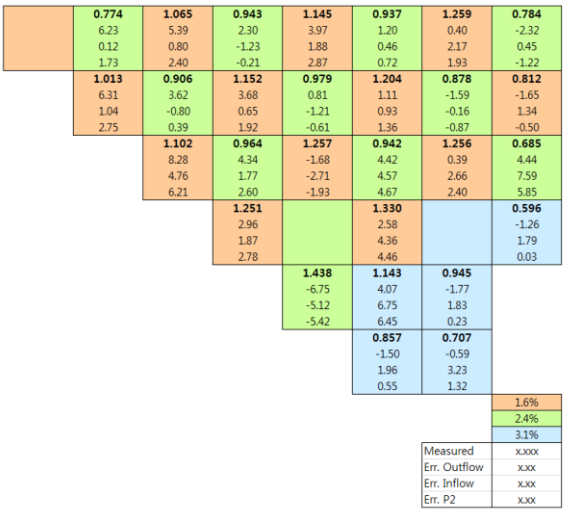

Fig. 9. BEAVRS measured assembly in-core detector signals and relative errors of each method

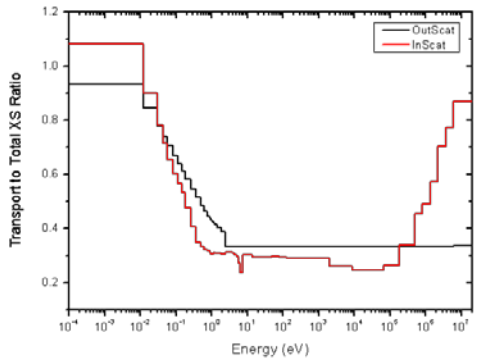

Fig. 10. Transport cross sections relative to the total cross sections for hydrogen

5. Conclusions

The higher order anisotropic scattering treatment capabilities upto the third order were implemented successfully in the nTRACER direct whole core transport code. In addition, a unique method to generate the in-scattering based transport cross sections utilizing an assumed representative core flux spectrum was developed and implemented. It was demonstrated by a serious of the VERA benchmark calculations that the improved anisotropic treatments can resolve the significant error associated with the isotropic scattering treatment with the out-scattering based transport correction. Particularly, the large reactivity error greater than 500 pcm for the control rodded assembly lattices and the large over-prediction of the assembly power in the core interior by more than 5% can be removed effectively with these improvements. The cost of about two-time longer computing times with the P2 treatment can be effectively offset by the use of in-scattering based transport cross sections. However, it is desired to establish more efficient higher order scattering treatment module in order not to use the isotropic scattering treatment at all to assure better accuracy in all the cases.

Acknowledgements

The authors thank Dr. Kang Seog Kim of Oak Ridge National Laboratory for informing the importance of anisotropic scattering near strong absorbers. This work was supported by National Research Foundation of Korea (NRF) Grant No. 2009-0083414.

REFERENCES

[1] A. Yamamoto, Y. Kitamura, and Y. Yamane, “Simplified Treatments of Anisotropic Scattering in LWR Core Calculations,” J. Nucl. Sci. Technol., 45, 217-229 (2008).

[2] Y. S. Jung, C. B. Shim and H. G. JOO, Practical Numerical Reactor Employing Direct Whole Core Neutron Transport and Subchannel thermal/hydraulic solvers, Annals of Nuclear Energy 62 357-374, 2013.

[3] N. Horelik and B. Herman, MIT Benchmark for Evaluation and Validation of Reactor Simulations, *MIT Computational Reactor Physics Group*, Rev. 1.1.1, 2013.

[4] A. T. Godfrey, Vera Core Physics Benchmark Progression Problem Specifications, Revision 3, CASL-U2012-0131-003, CASL, March 31, 2014.